

Automated Volumetric Intravascular Plaque Classification Using Optical Coherence Tomography

Ronny Shalev, Daisuke Nakamura, Setsu Nishino, Andrew M. Rollins,
Hiram G. Bezerra, David L. Wilson, Soumya Ray

■ An estimated 17.5 million people died from a cardiovascular disease in 2012, representing 31 percent of all global deaths. Most acute coronary events result from rupture of the protective fibrous cap overlying an atherosclerotic plaque. The task of early identification of plaque types that can potentially rupture is, therefore, of great importance. The state-of-the-art approach to imaging blood vessels is intravascular optical coherence tomography (IVOCT). However, currently, this is an offline approach where the images are first collected and then manually analyzed an image at a time to identify regions at risk of thrombosis. This process is extremely laborious, time consuming, and prone to human error. We are building a system that, when complete, will provide interactive three-dimensional visualization of a blood vessel as an IVOCT is in progress. The visualization will highlight different plaque types and enable quick identification of regions at risk. In this article, we describe our approach, focusing on machine-learning methods that are a key enabling technology. Our empirical results using real OCT data show that our approach can identify different plaque types efficiently with high accuracy across multiple patients.

Imaging techniques are a key tool in the diagnosis of disease. X-rays, ultrasound, CAT, and PET scans are now routinely used as a preliminary step to determine the extent of a disease and the need for and type of treatment (Tearney et al. 2006). These techniques generate vast quantities of data. The images that are produced must typically be analyzed by trained clinicians. This is extremely labor intensive, expensive, and can be prone to error. Thus, there is a need for, and an opportunity to, improve the quality of health-care systems by developing automated aids to assist in this process. Given the patient-critical outcomes of the image-analysis process, a human analyst must always remain in the loop. However, it may be possible to reduce the labor involved, and thereby the costs to the patient, using such systems. Further, a well-designed system may also reduce errors, potentially saving lives.

There are rarely well-defined, crisp guidelines that can be used, for example, to separate healthy tissue from diseased. Therefore, such image analysis tasks are often formulated as machine-learning problems. Here, a collection of images annotated by experts is used as data to train a classifier, which is then used to help annotate a new image. Typically, this system will present a rank-ordered list of image regions to the human analyst for verification or correction.

In our work, we focus on image analysis for coronary artery disease (CAD). This is a leading cause of death worldwide. An estimated 17.5 million people died from a cardiovascular disease in 2012, representing 31 percent of all global deaths. Of these deaths, an estimated 7.4 million were due to coronary heart disease and 6.7 million were due to stroke (Mendis, Puskas, and Norrving 2011). Although this is such a common disease, the underlying causes are quite complex, and it is only recently that an imaging technique that can help identify the disease mechanism clearly has been developed. This tech-

nique is called intravascular optical coherence tomography (IVOCT). In the following sections, we describe in detail CAD, the prior state of the art in imaging for CAD, and the IVOCT technique.

Like many other imaging techniques, a major issue with IVOCT is that it can produce more than 500 images in a single scan, resulting in an explosion of image data. This can be difficult and labor intensive to analyze manually, taking up to one hour of examination for each image by a trained analyst, of which there are not many, given the recency of the technique (Lu et al. 2012). This often precludes measurements from every frame, and plaque classification is not done because it is infeasible in terms of time. Further, this manual process is also prone to error. In prior work (Lu et al. 2012), our group has found evidence of up to 5 percent intra- and 6 percent inter-rater variability among analysts looking at these images.

The goal of our work is to enable an effective detection and diagnosis of CAD, which is a necessary precursor for effective treatment. We aim to build a tool to do this in three ways: (1) reduce the effort involved, (2) improve the accuracy of disease mechanism identification, and (3) make the diagnosis available as early in the process as possible. The prevalence of CAD means achieving these goals can have a major impact on health worldwide.

We anticipate fulfilling our goals in two steps. In the first step, reported in this article, we develop an automated method to process a single image generated by IVOCT scans. We demonstrate that it is accurate and efficient on real IVOCT data and that analysts can use the output to greatly reduce their annotation effort. In the second step, our goal is to integrate this approach into a real-time visualization that accompanies an IVOCT scan. These images will be annotated with different detected plaque types and will be used for rapid identification of high-risk regions for intervention, management and guidance.

Cardiovascular Artery Disease (CAD)

In this section, we discuss CAD and the state of the art in its diagnosis and treatment.

The underlying disease process in the blood vessels that results in coronary heart disease (heart attack) is known as atherosclerosis. For many years, it was thought that the main cause of a heart attack was the buildup of fatty plaque within an artery leading to the heart. With time, the plaque buildup would narrow the artery so much that the artery would either close off or become clogged by a blood clot (stenosis). The lack of oxygen-rich blood to the heart would then lead to a heart attack. However, these types of blockages cause only about 3 out of 10 heart attacks (Virmani et al. 2000).

Researchers are now finding that many people who have heart attacks do not have arteries severely

narrowed by plaque (Falk 1983). In fact, vulnerable plaque may be buried inside the artery wall and may not always bulge out and block the blood flow through the artery. This is why researchers began to look for, potentially, a different cause. What they found was that a thin protective fibrous cap (FC) overlying an atherosclerotic plaque (lipid pool) may rupture, triggering the formation of a blood clot, which may eventually lead to an acute event such as heart attack.

Current state-of-the-art treatment of the disease focuses on blood vessel narrowing by means of percutaneous interventions (PCIs). PCI is a procedure that uses a catheter (a thin flexible tube) to place a “stent” to open up blood vessels in the heart that have been narrowed by plaque buildup (stenosis). A stent is a flexible tube that reinforces the blood vessel wall. This needs significant imaging support to determine how, where, or even if it should be done. For example, the presence of significant calcification in the vessel may prevent the stent from being placed or from functioning as intended, triggering additional procedures to remove the calcium or aborting the procedure. On the other hand, if there is a lipid pool that may rupture, a physician can extend a stent to seal off the affected area or at least avoid placing the stent edge in a lipid region, an occurrence that raises the risk of a tear or damage to the inner wall or lining of an artery. These examples highlight the need for a reliable imaging technique with suitable resolution to identify plaque at high resolution (for example, thickness of vulnerable fibrous cap $\ll 65 \mu\text{m}$).

The current standard intravascular imaging modality is intravascular ultrasound (IVUS). IVUS is a medical imaging methodology that uses a catheter with a miniaturized ultrasound probe attached to the distal end of the catheter. The proximal end of the catheter is attached to an ultrasound device. The IVUS machine produces a detailed cross-sectional image of the vessel wall and plaque as a gray level intensity image. An example of the IVUS two-dimensional (2D) cross-sectional image is shown in figure 1, which shows the plaque and vessel wall from which the ultrasound wave bounces off.

When analyzing the 2D image generated by the IVUS machine, it is possible to quantify, limited to the IVUS resolution, the lipid plaque and the fibrous plaque. However, quantification of the total amount of vessel calcification by IVUS is problematic in that its resolution is low and it cannot measure the distance between the superficial calcium and the vessel boundary, nor can it assess the thickness of calcium (Mintz et al. 1995).

Intravascular Optical Coherence Tomography (IVOCT)

In this section, we introduce IVOCT and describe its

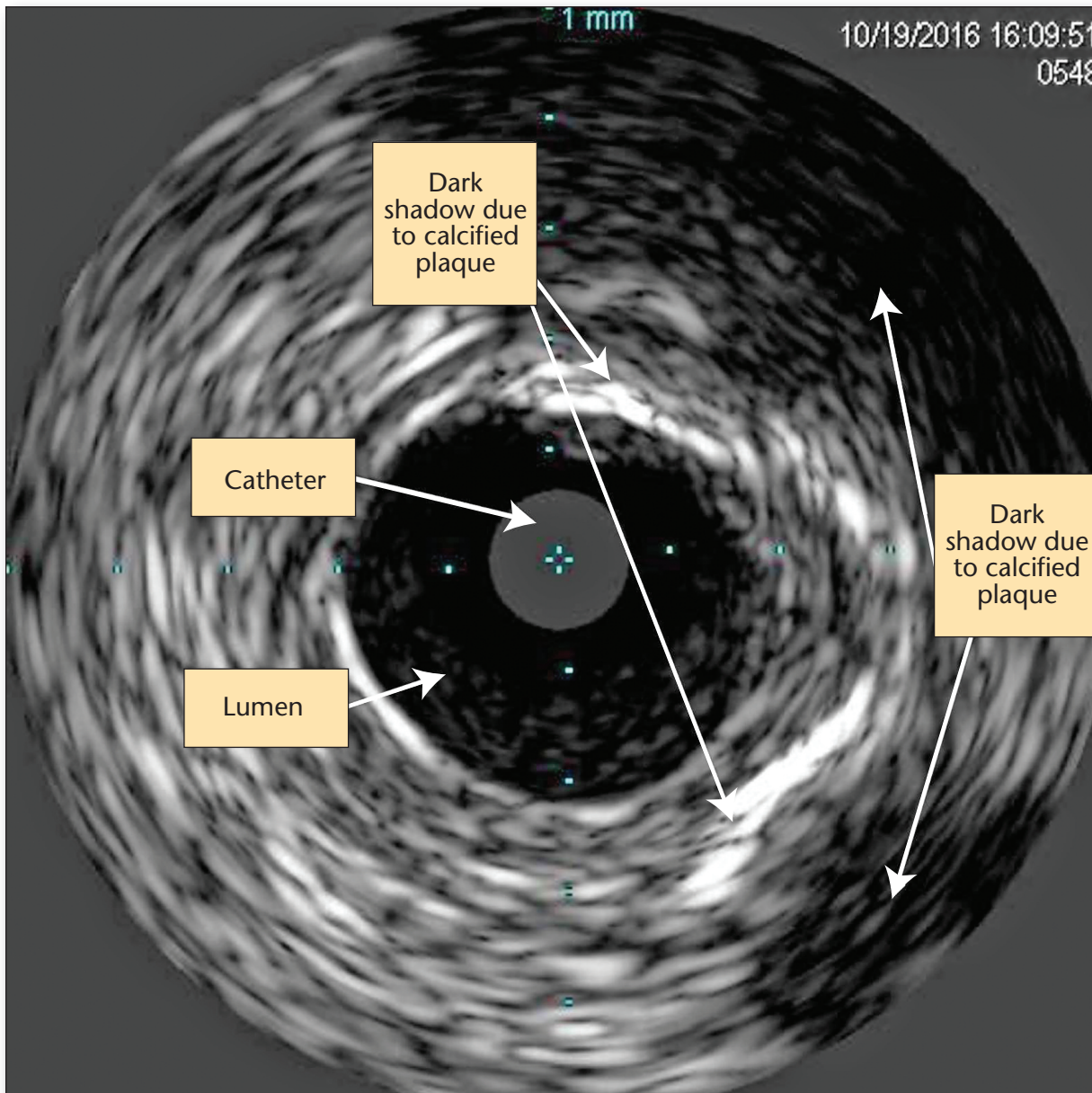


Figure 1. Intravascular Ultrasound Image.

advantages relative to IVUS. Intravascular optical coherence tomography uses the same concept of imaging, only it uses light instead of ultrasound waves. The underlying concept of OCT is similar to that of ultrasound; by measuring the delay time of optical echoes reflected or back scattered from sub-surface structures in tissues, we can obtain structural information as a function of depth within the tissue (Tearney et al. 2012).

In IVOCT, we obtain cross-sectional images by inserting a flexible imaging probe (catheter) into the blood vessel to be imaged. The catheter has an optical fiber coupled to a lens and microprism. The microprism reflects the OCT beam perpendicular to

the catheter's longitudinal direction and captures the light that is back scattered from that tissue (the reflected beam is referred to as an *A-Line*, figure 2a). The probe is then rotated and pulled back. This pull-back creates a two-dimensional image (referred to as polar or $r-\theta$ image) by assembling successive A-lines next to each other resulting in an image shown in figure 2b. This image is then transformed to Cartesian coordinates to produce the image shown in figure 2c. A typical pullback contains 271 images covering 54 mm and an image contains 504 A-lines.

Different tissues have different qualities that influence the back reflectance. The longer the distance traveled, the longer the delay in returning to a detec-

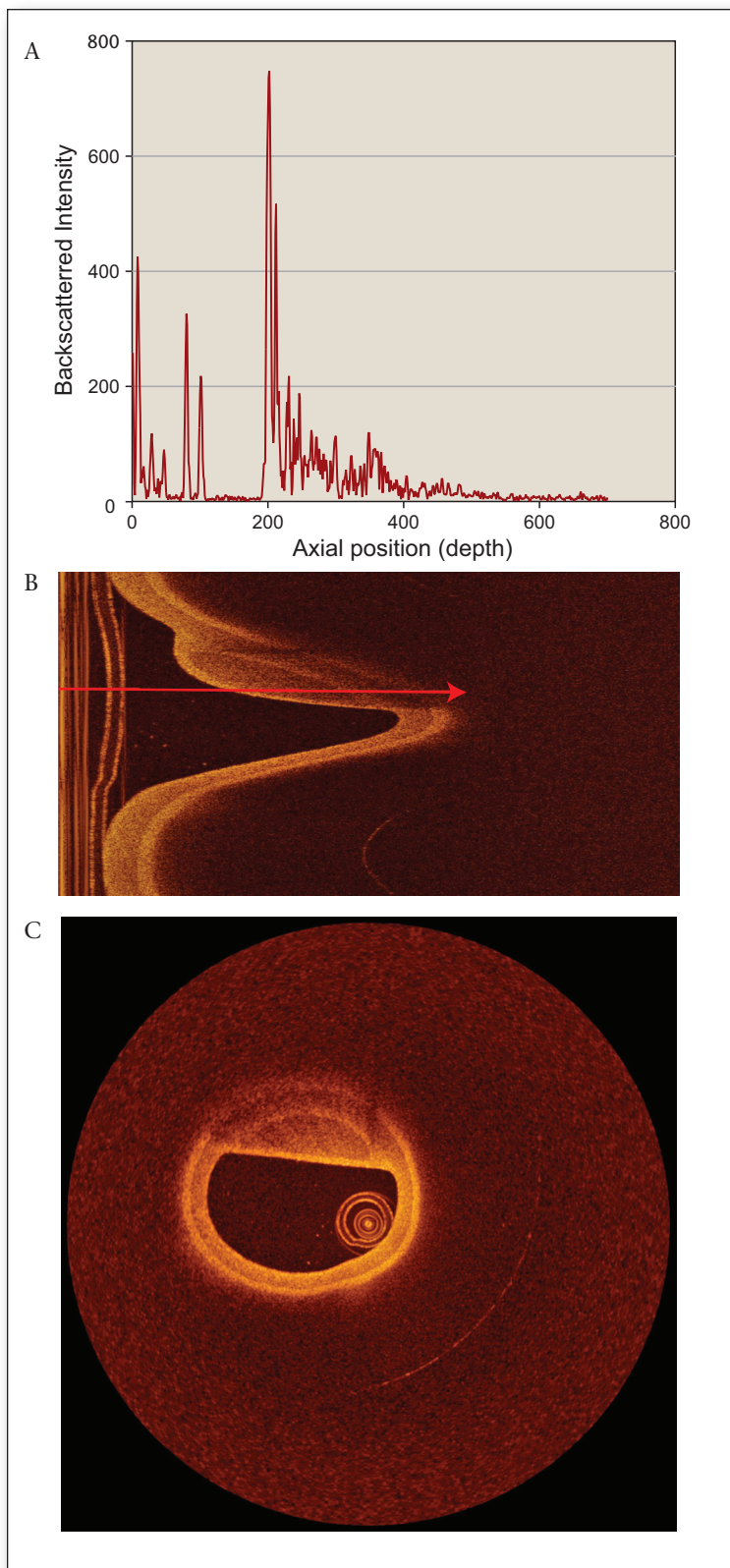


Figure 2. Intravascular OCT Image Generation Process

a) Back-scattered intensity of a single A-line. (b) Polar (r - θ) image (the red line is the A-line in a). (c) The polar image converted to the more human readable x - y .

tor. The delay in the returning light from deeper structures compared with shallow structures is used to reconstruct images.

Since its approval for clinical use, IVOCT has become an invaluable tool for vascular assessments due to its high contrast and microscopic resolution (5–15 μm), which is superior to other in vivo imaging modalities such as IVUS. To exemplify the difference in the output of IVUS and IVOCT, we show in figure 3 what a calcified cross section might look like using both modalities.

A key advantage of IVOCT over IVUS is that it is able to distinguish key types of plaque (Yabushita et al. 2002) and aid in assessment of new coronary artery stent design (Lu et al. 2012, Wang 2012). This is important because the presence of calcium is the strongest factor affecting “stent expansion,” a well-documented metric for clinical outcome (Fujimoto, Nakamura, and Yokoi 2012; Nishida et al. 2013). IVOCT provides the location, circumferential extent, and thickness of calcium. Second, there can be a geographic miss, where the stent either misses the lesion along its length or is improperly expanded, affecting its ability to stabilize the lesion and/or provide appropriate drug dosage. This has a well-documented impact on recurrence of narrowing (Costa et al. 2008). Plaque dissections at the edge of a stent (when a stent’s length does not fully cover the plaque along the vessel) clearly visible in IVOCT were detected by angiography in only 16 percent of cases (Chamie et al. 2013). Edge dissection (that is, when the edge of the stent lies on top of a plaque) happens almost exclusively in areas where the calcium/lipid plaque is not evenly distributed around the lumen circumference (Chamie et al. 2013), characteristics only available with intravascular imaging. Under IVOCT guidance, one can use a longer stent or apply a second stent to reduce effects of this geographic miss. Third, plaque sealing is the treatment of a lesion that may appear vulnerable and may rupture, under intravascular imaging. Because approximately 50 percent of coronary events after stenting happen at these remote, nonstented sites, plaque sealing is an attractive concept under investigation in trials. IVOCT’s high sensitivity for lipid plaque will be advantageous for guidance of plaque sealing.

For the reasons mentioned, we focus on analyzing IVOCT images for CAD. Next, we describe how we represent these images in order to train a classifier from them, followed by a detailed experimental evaluation.

Representing an IVOCT Image

In order to build our system, we need to identify different plaque types in IVOCT images automatically and accurately. In this section, we describe image characteristics that are key to identifying different plaque types. In constructing our features we use the

qualitative description of the different plaques' characteristics in prior work (Yabushita et al. 2002) described below. This also provides the ability to interpret results in a meaningful way.

A *fibrous plaque* (figure 4a) has high back scattering and the region has relatively homogeneous intensity values. We see that the average intensity is high (bright). Likewise, the intensity is not attenuated much along the A-line (Gargesha et al. 2015).

A *lipid plaque* (figure 4b) is a low-intensity region with poorly delineated borders, a fast IVOCT signal drop off, and little or no OCT signal back scattering, within a lesion that is covered by a fibrous cap. We see that the intensity starts very bright and decreases quickly along the A-line (Gargesha et al. 2015).

A *calcified plaque* (figure 4c) appears as a low intensity or heterogeneous region with a sharply delineated border (leading, trailing, and/or lateral edges). Calcium is darker than fibrous plaque with greater variation in intensity level.

Based on this description, we construct a set of eight (real-valued) features for each pixel in the image. We compute these features using a three-dimensional (3D) neighborhood centered on the pixel of interest. The third dimension comes from neighboring images (human analysts will often use adjacent images when annotating an image). In these features, σ represents the standard deviation of the intensity values within a 3D neighborhood.

Distance to Lumen (D_l): This is a measure of the distance of the center pixel from the lumen border (that is, the wall of the blood vessel). This feature helps identify lipid plaques since they are typically within a fibrous plaque.

Beam Penetration (D_d): This is a measure of the length of the beam from the lumen border to the back border (the border beyond which the near infrared beam does not reach and the signal is at baseline). It depends on tissue type, thus can distinguish between plaques. This feature is invariant for pixels across an A-line but varies across A-lines.

Mean Intensity (I): This represents the average signal intensity of the different plaque types within the 3D neighborhood. As can be seen in figure 4, this is a very distinctive feature.

Homogeneity (H): This is a local coefficient of variation, σ/I . It helps in distinguishing between heterogeneous intensity regions and homogeneous intensity regions.

Relative Smoothness of Intensity (S): This is defined as $S = 1 - 1/(1 + \sigma^2)$. S is 0 for constant intensity regions and it approaches 1 for large deviations in intensity values.

Entropy (E): Entropy is another measure of the variability of the signal intensity within the respective plaque type regions. To compute it, we construct a histogram of the intensity distribution within a 3D neighborhood, convert it to a probability distribution, and then estimate its information content.

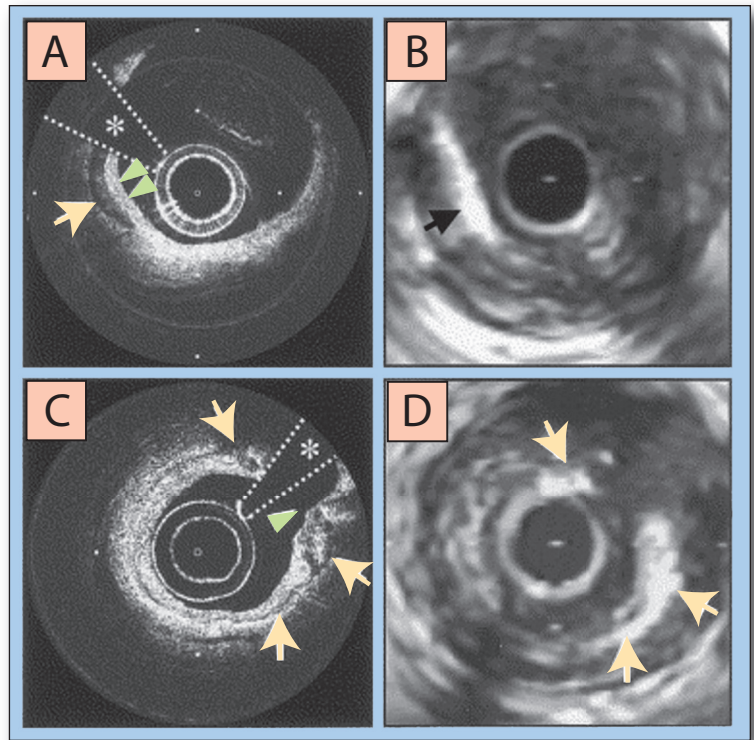


Figure 3. Calcific Coronary Plaques.

Imaged in vivo by optical coherence tomography (OCT) (A, C) and intravascular ultrasound (IVUS) (B, D). (A) This OCT image shows a well delineated, heterogeneous, signal-poor region corresponding to a macrocalcification (A, arrow), also seen in the corresponding IVUS image (B, arrow). A signal-rich fibrous band (A, two arrowheads) overlying the calcification is easily identified in the OCT image but is obscured by a saturation artifact in the IVUS image. (C) A thin layer of circumferential calcification is seen in this OCT image (arrows) as a well-defined, heterogeneous, signal-poor region within the vessel wall. A side-branch (arrowhead) can be seen adjacent to the guidewire artifact (*). (D) The extent of the calcifications (arrows) and their relation to the surrounding fibrous components of the plaque are not as clearly seen in the corresponding IVUS image. The borders of the guidewire (*) artifact are marked by dotted lines in A, C. Tick marks, 1 mm. (Source: Jang et al. 2002).

Similar features as these are often used in image-processing applications (Gonzalez, Woods, and Eddins 2009). The final two features we use are optical parameters.

Attenuation Coefficient, μ_t — This feature measures the rate at which the signal intensity drops off within the tissue. Calcified plaque has lower attenuation, and as a result, IVOCT can see deeper into these tissues compared to lipid, where IVOCT does not see as deeply. For this reason, the attenuation coefficient (or penetration depth) gives useful information about plaque types.

Incident Intensity, I_0 — This represents the back scattering characteristics of the plaque at the point where the light touches it. This feature is excellent at distinguishing fibrous plaques, which are very reflective.

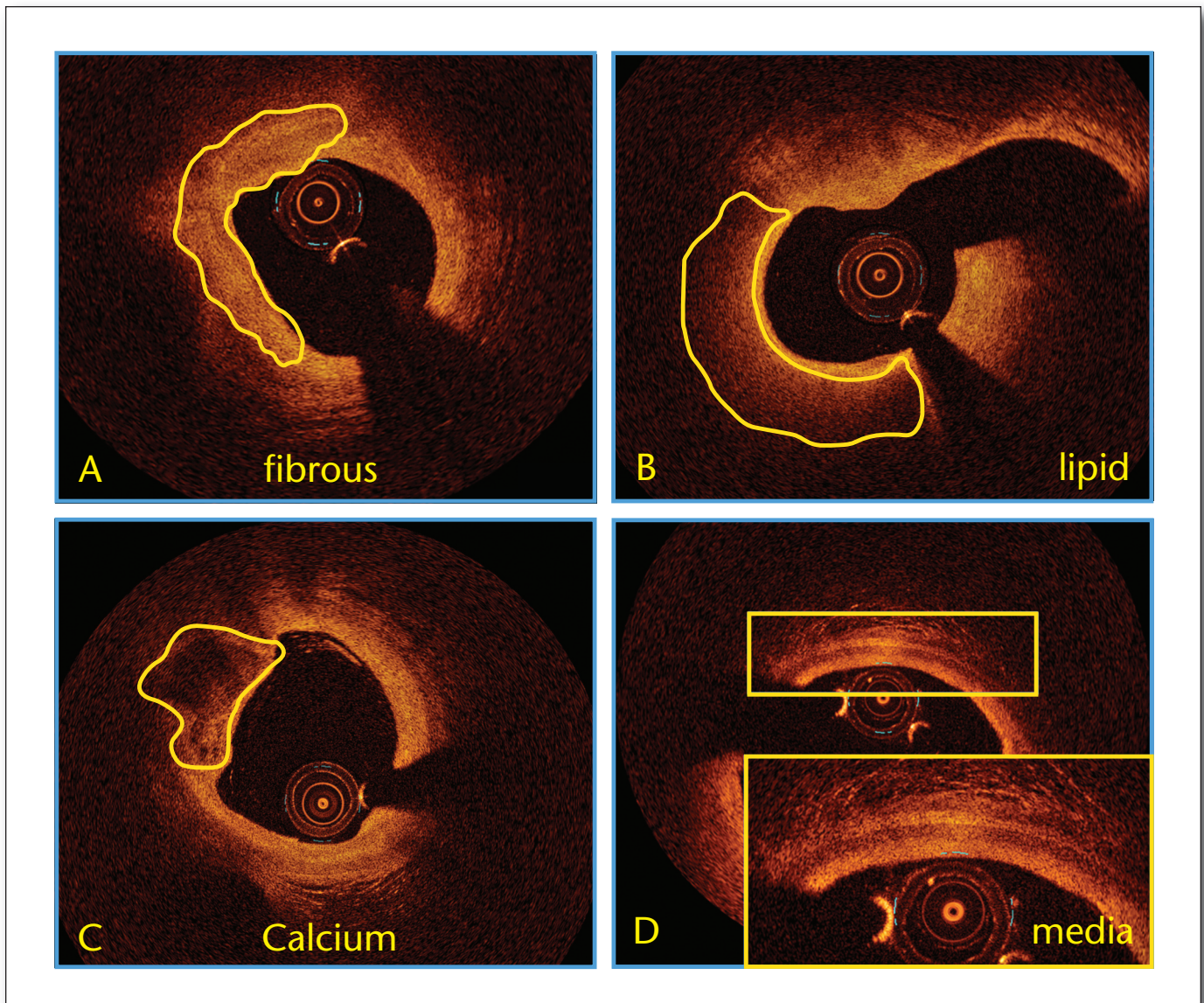


Figure 4. Appearance of Plaque Types in Clinical Images.

A is fibrous, B is lipid, and C is calcium. D shows the appearance of a normal blood vessel wall, which has layered structure.

These features are based on models of light transmission and reflectance. We verified our models by fabricating phantom (realistic imitations) blood vessels with known plaque types and checking the estimates against measured values in these cases.

The Plaque-Type Classifier

After extracting features from pixels in our IVOCT images, we then train a support vector machine (SVM) (Cristianini and Shawe-Taylor 2000) for classification of the individual pixels. The SVM is a state-of-the-art classification method. It is theoretically well founded and robust to noise in the data, which is a desirable property.

A second desirable property of the SVM is its ability to construct nonlinear classifiers through the use of kernel functions. A kernel function implicitly maps the input data to a possibly high dimensional space, where it learns a linear classifier. Since this mapping is done implicitly (that is, we never actually construct the high-dimensional feature vector), the procedure is computationally efficient. In our work, we use a radial basis function (RBF) kernel, which is a commonly used kernel.

The SVM is a binary classifier. Given that we are interested in classifying three different plaque types, we use a one-versus-rest (OVR) approach for multi-class classification. This produces three binary classifiers, one treating each class as positive and the oth-

ers as negative. During classification, each new example is classified by all three classifiers. If more than one classifies the point as positive, it is associated with the label corresponding to the classifier with the maximum margin.

There are two parameters that must be input to the SVM: C , the regularization parameter that trades off margin size and training error, and γ , the RBF kernel's bandwidth. In our experiments, we select these parameters using an internal fivefold stratified cross-validation loop and a two-dimensional grid search.

Image Data Sets

The clinical images (in vivo) that we used for evaluating our approach were selected from a large database of manually analyzed IVOCT images obtained in a clinical setting. Images were collected on the C7-XR system from St. Jude Medical Inc., Westford, MA. It has an OCT swept source that has a 1310 nm center wavelength, 110 nm wavelength range, 50 kHz sweep rate, and ~12 mm coherence length. The pullback speed was 20 mm/s and the pullback length was 54 mm. The images consist of 35 IVOCT pullbacks of the left anterior descending (LAD) and the left circumflex (LCX) coronary arteries of patients acquired prior to stent implantation, with a total of 287 images across 35 patients. An expert cardiologist on our team then labeled volumes of interest (VOIs) as belonging to one of the three plaque types in the images. The expert marked the VOIs of a particular plaque type using freehand brush strokes. On the clinical images the expert annotated 311 VOIs (roughly equal number from each plaque type). VOIs were of various sizes and shapes. Most consisted of 2–5 image frames, 50–200 A-lines, and 20–50 sample points in each A-line.

A concern with the images is that the image annotations we train with are provided by an expert and so could contain errors. To evaluate the performance of the trained classifier on ground truth, we created a second data set using cryo-imaging from cadaver samples (Salvado et al. 2006). The system serially sections and acquires micron-scale color images using different lighting wavelengths (figure 7, depicted later in this article, left column, bottom row shows an example of lipid plaque obtained this way) and autofluorescence microscopy images along the vessel (figure 7 left column, top row shows a calcified lesion obtained this way). Visualization software is then used on the cryo-images to generate microscopic resolution color/fluorescence volume renderings of vessels, in which plaque architecture and components are fully preserved (Nguyen et al. 2008, Prabhu et al. 2016). This provides an accurate depiction of the vessel without the limitations of standard histological fixation and processing (shrinkage, spatial distortion, missing calcifications, missing lipid pools, tears, and so on). Most importantly, this provides 3D validation

for volumetric IVOCT pullback. Furthermore, in cases where plaque type may be ambiguous, the system enables acquisition of standard cryo-histology.

We acquired a set of 106 such cryo-images. Note that, since these are ex vivo, we do not use these images for training our classifiers but use them to validate the results. We call these images “cryo-images” below to distinguish them from the previous set.

Empirical Evaluation

We now describe experiments to test our hypothesis that the system we described will be able to accurately and efficiently classify different plaque types from IVOCT images.

We preprocess all images for speckle noise reduction, baseline subtraction, catheter optical system correction, and catheter eccentricity correction. We segment the lumen and the back border using dynamic programming. To do this, we use a cost function from prior work (Wang 2012). An example of the results of the back-border segmentation is shown in figure 5 in both the r - θ view and the x - y view. Segmenting the image in this way is important because (1) the regions of interest are contained between these borders and the rest of the pixels do not contain any relevant information, and (2) it enables us to properly compute the distance to the lumen and the beam penetration depth discussed previously, which are important signals for different plaque types.

Next, we generate features by scanning the annotated VOIs in the image pixel by pixel. For each pixel, we construct a $7 \times 11 \times 3$ neighborhood (0.035mm x 0.055mm x 0.6mm) around it. As long as the neighborhood is within the VOI, the features of the box are computed as explained above and the values are assigned to the pixel. In the cryo-images we generated features for all pixels between border regions in a similar way.

For cross validation we use the processed images with a leave-one-pullback-out strategy. Here, in each iteration, we hold out all the data from one pullback as the test set and use the remaining 34 pullbacks as the training set. This mimics practical usage where the system will operate on novel pullbacks and is more stringent than using random folds. In a second experiment, we ran the trained classifiers on the cryo-images (these were not used at all during training/cross validation). We ran our experiments on a 64-bit Windows 7 machine with third-generation Intel Core i7 and 16 GB RAM.

Results and Discussion

The receiver operating curves (ROC) for each OVR classifier from the cross-validation experiment is shown in figure 6. The summary statistics are shown in table 1, where the accuracy, sensitivity, and specificity are noted at the optimal operating point along

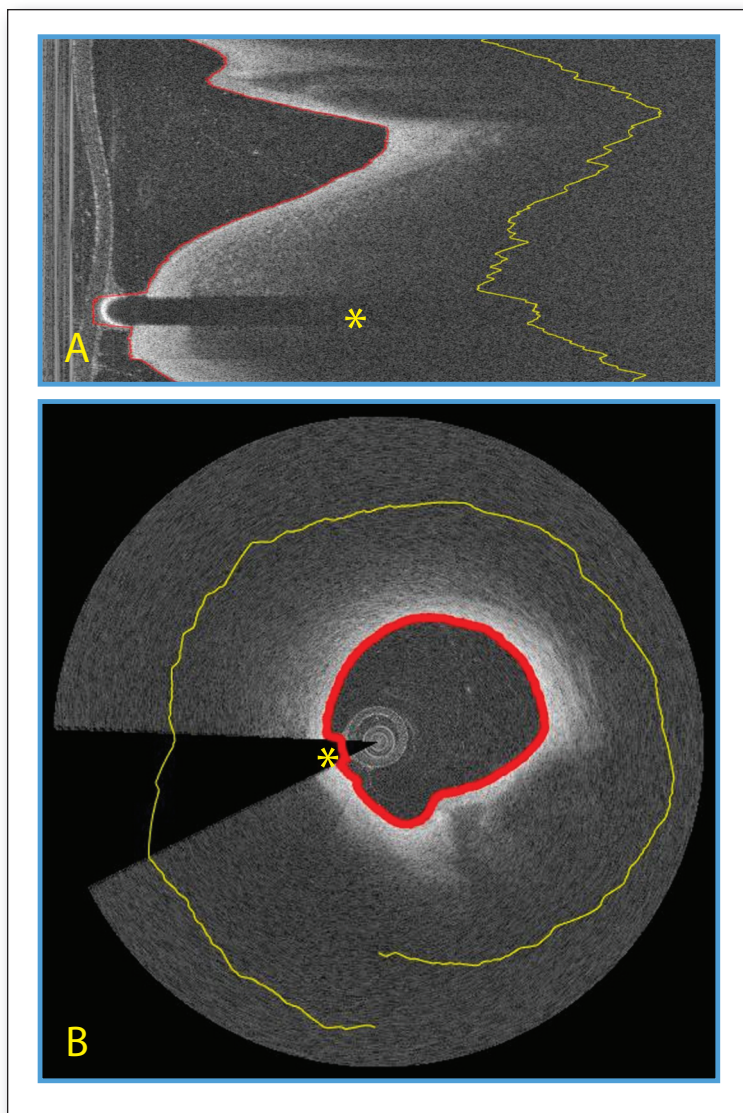


Figure 5. Results of the Back-Border Segmentation.

An illustration of back-border segmentation (yellow line) along with lumen segmentation (red line) in a typical clinical image in both views. (a) is the polar image and (b) is the x - y image. The yellow line is broken due to view conversion. Asterisk marks the guide-wire shadowing artifact.

	Calcium	Lipid	Fibrous
Accuracy	92.2 ± 6.28%	96.95 ± 2.79%	96.17 ± 4.0%
Sensitivity	93.0 ± 2.58%	98.95 ± 2.35%	94.28 ± 5.23%
Specificity	96.5 ± 3.39%	93.65 ± 2.77%	95.89 ± 2.18%
AUC	0.9837	0.9947	0.9959

Table 1. Performance Measures.

Area under ROC and the accuracy, sensitivity, and specificity at the optimal operating point on the ROC curves.

the curves. The ROC describes the system’s behavior for a range of confidence threshold settings and enables the cardiologist (the end user) to decide on weighting the false positives (FPs) and false negatives (FNs) unequally (a very desirable property according to our expert).

The overall accuracy results, averaged over 35 folds, are shown in table 2. As can be seen from all of these results, our approach has excellent accuracy for all three plaque types. In fact, across the 35 folds, the median accuracy for all three plaque types is 100 percent, indicating that our classifiers are able to perfectly separate the plaque types using the features we designed. In a few folds, the accuracy is lower than 100 percent. We conjecture that this is because some pullbacks have many more images associated with them than others. When such a pullback is held out, the training set size decreases in size and yields a classifier with lower accuracy.

In the second experiment, we ran our trained classifier on the cryo-images. We also ran a baseline approach following Ughi et al. (2013). This approach uses beam-attenuation estimates from a layer model applied to single A-lines and 2D texture and geometric measures as features for classification with the added requirement of manual region of interest selection for analysis. These results are shown in table 3. Here the “Other” row corresponds to pixels in these images that belong to none of the three plaque types. The accuracy of the approach in this case is lower, possibly because these are ex vivo images, which have somewhat different characteristics from the training set. However, our approach still outperforms the state of the art. Further, these values are still at a very useful level according to our expert. In particular, cardiologists now divide an image into quadrants and simply state whether a quadrant contains a certain plaque type. If we use this as a performance measure, our current approach has perfect accuracy on the cryo-images.

The results also indicate that in some cases some plaque types may be confused with others. For example, the average intensity of a lipid region may be very close to that of calcium. However, they may still be separable due to the fact that the lipid’s attenuation coefficient is much higher.

To confirm our intuitive understanding of the plaques’ characteristics we performed a leave-one-feature-out experiment. In this experiment, we ran the classifier using all of the features and noted the accuracy measures (as shown in table 2). We then removed each feature at a time to see the impact on the accuracy. We found that removing the attenuation parameter had the biggest impact on the lipid accuracy, reducing it down to 92.4 ± 8.87 percent, while removing the average intensity feature had a significant effect on the fibrous’ accuracy and uncertainty (down to 95.2 percent ± 10.75).

In addition to high accuracy, our approach is also efficient at classification. Each test fold (on average

200,000 data points) was classified in 0.366 seconds by our implementation. This facilitates future real-time usage.

Finally, we consider whether an automatic classification procedure such as this can be useful in reducing the amount of time taken to process images in a clinical setting. In an initial experiment, we found that cardiologists would spend approximately five hours analyzing a section of a blood vessel. We then created a tool (figure 8) with our classifier built in. The screen of this graphic user interface (GUI) is divided into two main regions. The leftmost region contains the tools provided to the user. There, the user can select which view is most informative, adjust image contrast and/or window level, and so on. The right region is the work area where the user can interact with any of the views, slide along the pullback to focus on the cross section of interest, make measurements, create annotations, and more. The cardiologist would run the classifier for a new image and then, using the interactive tools, analyze the results and correct some of the errors in the predictions.

The process, which the cardiologist follows, can be described by following the process used in order to annotate, classify, validate, and clean classification results as shown in figure 7. In this figure, the leftmost column shows cryo-images (Roy et al. 2009) while the second column from the left shows the IVOCT images. Using the annotation function of the plaque analysis tool, the expert would annotate the image pixels as belonging to either calcium, lipid, fibrous, or something else (used during training). The third column from the left shows the result of this annotation. It shows a mask, the same size as the image itself, that indicates the location of each plaque using colors. The next step includes running the classifier, the results of which are shown in the fourth column from the left. These results after pre-processing to remove isolated artifact predictions are presented to the cardiologist (rightmost column).

We found that this process took at most an hour, a reduction of 80 percent. This effort reduction indicates that improving the tool (figure 8) will make it deployable in the near future.

Conclusion and Future Work

In this article, we have discussed an important emerging application: an automated approach for early plaque detection in blood vessels. Our approach analyzes IVOCT images to solve this task. Using a carefully designed feature set, we show that an SVM with an RBF kernel is a high-accuracy classifier for this task. Our results are of significant impact on this important problem (Wagstaff 2012) with implications for early diagnosis of cardiovascular disease. Now, for the first time, to our knowledge, it is possible to perform complete plaque analysis automatically, enabling not only treatment planning for

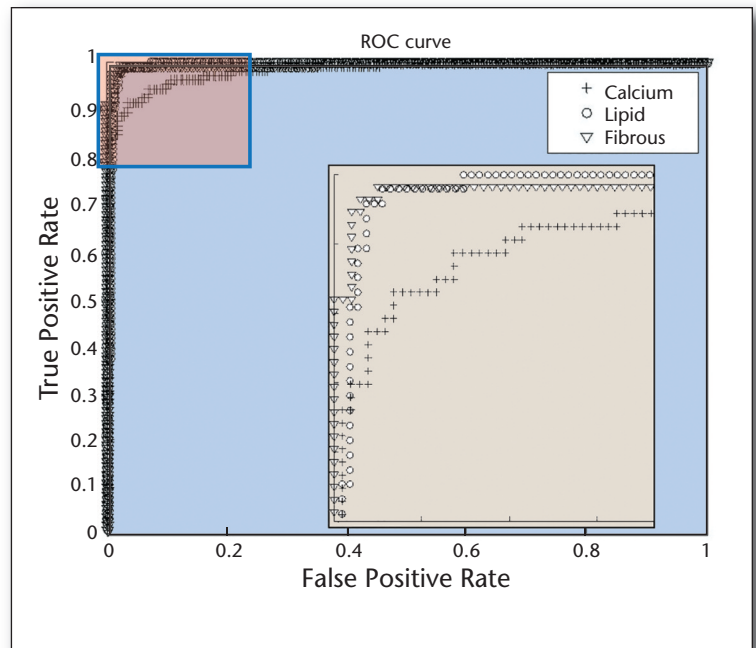


Figure 6. ROC Curve for All Three Plaque Types.

Area under the curve (AUC) values are 0.9837, 0.9947, and 0.9959 for calcium, lipid, and fibrous, respectively.

	Accuracy	Median Acc.
Overall	90.70 ± 8.28%	
Calcium	92.14 ± 10.74%	100%
Lipid	96.40 ± 8.87%	100%
Fibrous	100% ± 0.0%	100%

Table 2. Accuracy Results for Leave-One-Pullback-Out Experiment.

	Our Approach	Baseline
Overall	81.15%	69.4%
Calcium	97.62%	66.88%
Lipid	87.65%	67.07%
Fibrous	97.39%	77.95%
Other	77.96%	30.46%

Table 3. Accuracy Results for Cryo-images.

plaque modification in real time but also to provide enough information to perform studies on the effects of various treatments of vulnerable plaque as well as offline assessment of drug and biologic therapeutics.

In future work we will develop a complete software suite for automated plaque characterization, creating

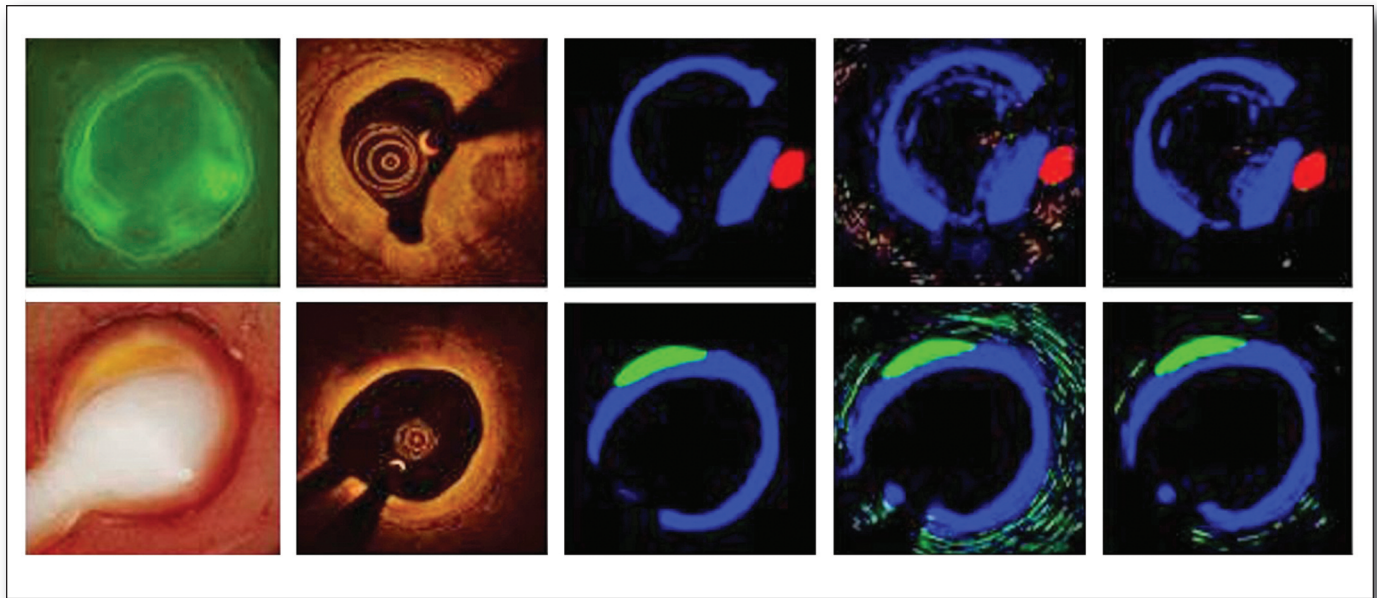


Figure 7. Example of Validation Analysis.

Top row images (from left to right): cryo-image fluorescence, IVOCT, expert annotation of IVOCT guided by registered cryo-image, results of automated classification, and automated classification after noise cleaning. In the bottom row, image data from a different vessel segment are shown with the exception that the fluorescence image is replaced by the color cryo-image. Calcium, fibrous, and lipid are labeled red, blue, and green respectively. Note the good correspondence between the third and fifth columns, indicating good classifications.

a powerful tool for live-time treatment planning of coronary artery interventions by adding functionality such as integration with a real-time 3D visualization module that will be able to quantify (volume, area covered, and others) the presence of calcified regions. An example of such visualization is shown in figure 9, which is implemented by stacking the output of multiple 2D images.

This can help in decision making regarding stent implantation and preimplantation treatment, or plaque remodeling (for example, directional atherectomy). We also plan to add an explanatory module to help explain the automated classification process to the interventional cardiologists and to accept feedback in an active learning environment. Finally, we will develop an easily accessible web-based tool for offline analysis of IVOCT images.

We expect that such a tool will be used by entities requiring fast analysis that can provide data useful for drug assessment, experimental therapeutics, and experimental medical devices.

Acknowledgments

This project was supported by Ohio

Third Frontier, and by the National Heart, Lung, and Blood Institute through grants NIH R21HL108263 and 1R01HL114406-01, and by the National Center for Research Resources and the National Center for Advancing Translational Sciences through grant UL1RR024989. These grants are collaboration between Case Western Reserve University and University Hospitals of Cleveland.

References

- Chamié, D.; Bezerra H. G.; Attizzani. G. F.; Yamamoto, H.; Kanaya, T.; Stefano, G. T.; Fujino, Y.; Mehanna, E.; Wang, W.; Abdul-Aziz, A.; Dias, M.; Simon, D. I.; Costa, M. A.; 2013. Incidence, Predictors, Morphological Characteristics, and Clinical Outcomes of Stent Edge Dissections Detected by Optical Coherence Tomography. *JACC Cardiovascular Interventions* 6(8): 800–813. doi.org/10.1016/j.jcin.2013.03.019
- Costa, M. A.; Angiolillo. D. J.; Tannenbaum, M.; Driesman, M.; Chu, A.; Patterson, J.; Kuehl, W.; Battaglia, J.; Dabbons, S.; Shamon, F.; Flieshman, B.; Niederman, A.; Bass, T. A. 2008. Impact of Stent Deployment Procedural Factors on Long-Term Effectiveness and Safety of Sirolimus-Eluting Stents (Final Results of the Multicenter Prospective STLLR Trial). *American Journal of Cardiology* 10(12): 1704–1711. doi.org/10.1016/j.amjcard.2008.02.053
- Cristianini, N., and Shawe-Taylor, J. 2000. *An Introduction to Support Vector Machines and Other Kernel-Based Learning Methods*. Cambridge, UK: Cambridge University Press.
- Falk, E. 1983. Plaque Rupture with Severe Pre-Existing Stenosis Precipitating Coronary-Thrombosis — Characteristics of Coronary Atherosclerotic Plaques Underlying Fatal Occlusive Thrombi. *British Heart Journal* 50(2): 127–134.
- Fujimoto, H.; Nakamura, M.; and Yokoi, H. 2012. Impact of Calcification on the Long-Term Outcomes of Sirolimus-Eluting Stent Implantation: Subanalysis of the Cypher Post-Marketing Surveillance Registry. *Circulation Journal* 76(1): 57–64.
- Gargasha, M.; Shalev, R.; Prabhu, D.; Tanaka, K.; Rollins, A. M.; Costa, M.; Bezerra, H. G.; Wilson, D. L. 2015. Parameter Estimation of Atherosclerotic Tissue Optical Properties from 3D Intravascular OCT. *SPIE Journal of Medical Imaging* 2(1): 14.
- Gonzalez, R. C.; Woods, R. E.; and Eddins, S. L. 2009. *Digital Image Processing Using MATLAB*. Knoxville, TN: Gatesmark Publishing.
- Jang, I. K.; Bouma, B. E.; Kang, D. H.; Park, S. J.; Park, S. W.; Seung, K. B.; Choi, K. B.; Shishkov, M.; Schlendorf, K.; Pomerantsev, P.; Houser, S. L.; Aretz, H. T.; Tearney, G. J.; 2002. Visualization of Coronary Atherosclerotic Plaques in Patients Using Optical

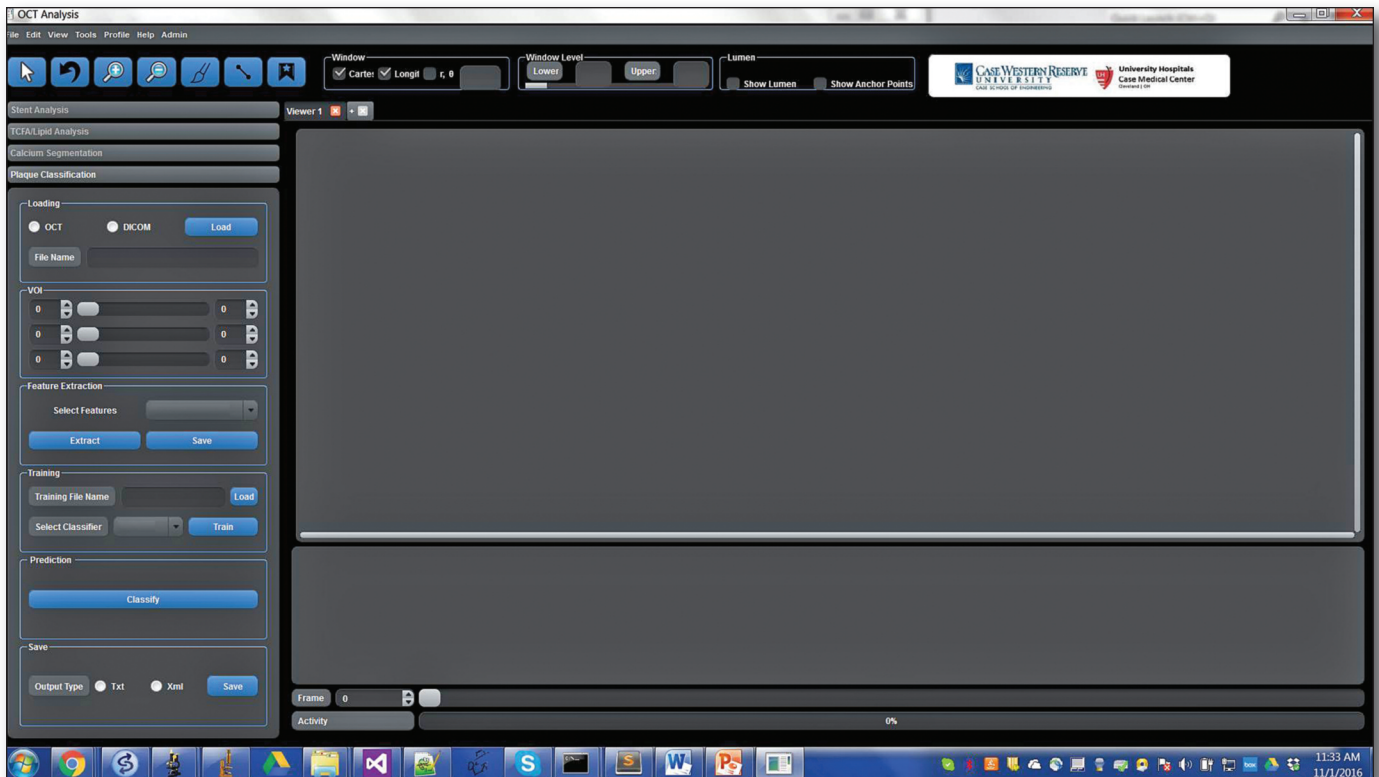


Figure 8. Graphic User Interface of Plaque Analysis Tool.

The left side provides various editing tools. On the right the tool provides views to be used by the interventional cardiologist.

Coherence Tomography: Comparison with Intravascular Ultrasound. *Journal of the American College of Cardiology* 39(4): 604–609.

Lu, H.; Garghesha, M.; Wang, Z.; Chamie, D.; Attizzani, G. F.; Kanaya, T.; Ray, S.; Costa, M. A.; Rollins, A. M.; Bezerra, H. G.; and Wilson, D. L. 2012. Automatic Stent Detection in Intravascular OCT Images Using Bagged Decision Trees. *Biomedical Optics Express* 3(11): 2809–2824.

Mendis, S.; Puska, P.; and Norrving, B. 2011. *Global Atlas on Cardiovascular Disease Prevention and Control*. Geneva, Switzerland: World Health Organization.

Mintz, G. S.; Popma, J. J.; Pichard, A. D.; Kent, K. M.; Satler, L. F.; Chuang, Y. C.; Ditrano, C. J.; Leon, M. B. 1995. Patterns of Calcification in Coronary Artery Disease. A Statistical Analysis of Intravascular Ultrasound and Coronary Angiography in 1155 Lesions. *Circulation* 91(7): 1959–1965.

Nguyen, M. S.; Salvado, O.; Roy, D.; Steyer, G.; Stone, M. E.; Hoffman, R. D.; Wilson, D. L. 2008. Ex Vivo Characterization of Human Atherosclerotic Iliac Plaque Components Using Cryo-Imaging. *Journal of Microscopy* 232(3): 432–441.

Nishida, K.; Kimura, T.; Kawai, K.; Miyano, I.; Nakaoka, Y.; Yamamoto, S.; Kaname, N.; Seki, S.; Kubokawa, S.; Fukatani, M.; Hamashige,

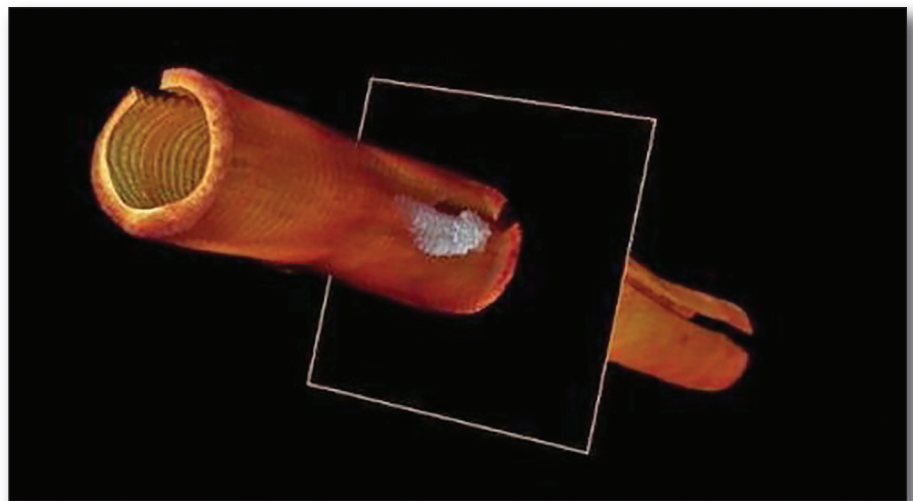


Figure 9. 3D Visualization of Calcified Region Within, Otherwise, Healthy Blood Vessel.

The white region indicates the presence of calcium (created using Amira). Best viewed in color.

N.; Morimoto, T.; Mitsudo, K. 2013. Comparison of Outcomes Using the Sirolimus-Eluting Stent in Calcified Versus Non-Calcified Native Coronary Lesions in Patients On-Versus Not On-Chronic Hemodialysis (From

the J-Cypher Registry) *American Journal of Cardiology* 112(5): 647–655.

Prabhu, D.; Mehanna, E.; Garghesha, M.; Brandt, E.; Wen, D.; van Ditzhuijzen, N. S.; Chamie, D.; Yamamoto, H.; Fujino, Y.; Alian,

- A.; Patel, J.; Costa, M.; Bezerra, H. G.; Wilson, D. L. 2016. Three-Dimensional Registration of Intravascular Optical Coherence Tomography and Cryo-Image Volumes for Microscopic-Resolution Validation. *Journal of Medical Imaging* (Bellingham) 3(2): 026004.
- Roy, D.; Steyer, G. J.; Gargasha, M.; Stone, M. E.; Wilson, D. L. 2009. 3D Cryo-Imaging: A Very High-Resolution View of the Whole Mouse. *Anatomical Record: Advances in Integrative Anatomy and Evolutionary Biology. The Anatomical Record.* 292(3): 342–351. doi.org/10.1002/ar.20849
- Salvado, O.; Roy, D.; Heinzel, M.; McKinley, E.; Wilson, D. 2006. 3D Cryo-Section/Imaging of Blood Vessel Lesions for Validation of MRI Data. *Proceedings of SPIE International Society of Optical Engineering* 6142(614214): 377–386. doi.org/10.1117/12.649093
- Tearney, G. J.; Jang, I. K.; and Bouma, B. E. 2006. Optical Coherence Tomography for Imaging the Vulnerable Plaque. *Journal of Biomedical Optics* 11(2): 021002-021002.
- Tearney G. J.; Regar, E.; Akasaka, T.; Adriaenssens, T.; Barlis, P.; Bezerra, H. G.; Bouma, B.; Bruining, N.; Cho, J. M.; Chowdhary, S.; Costa, M. A.; de Silva, R.; Dijkstra J.; Di Mario, C.; Dudek, D.; Falk, E.; Feldman, M. D.; Fitzgerald, P.; Garcia-Garcia, H. M.; Gonzalo, N.; Granada, J. F.; Guagliumi, G.; Holm, N. R.; Honda, Y.; Ikeno, F.; Kawasaki, M.; Kochman, J.; Koltowski, L.; Kubo, T.; Kume, T.; Kyono, H.; Lam, C. C.; Lamouche, G.; Lee, D. P.; Leon, M. B.; Maehara, A.; Manfrini, O.; Mintz, G. S.; Mizuno, K.; Morel, M. A.; Nadkarni, S.; Okura, H.; Otake, H.; Pietrasik, A.; Prati, F.; Räber, L.; Radu, M. D.; Rieber, J.; Riga, M.; Rollins, A.; Rosenber, M.; Sirbu, V.; Serruys, P. W.; Shimada, K.; Shinke, T.; Shite, J.; Siegel, E.; Sonoda, S.; Suter, M.; Takarada, S.; Tanaka, A.; Terashima, M.; Thim, T.; Uemura, S.; Ughi, G. J.; van Beusekom, H. M.; van der Steen, A. F.; van Es, G. A.; van Soest, G.; Virmani, R.; Waxman, S.; Weissman, N. J.; Weisz, G.; International Working Group for Intravascular Optical Coherence Tomography. 2012. Consensus Standards for Acquisition, Measurement, and Reporting of Intravascular Optical Coherence Tomography Studies. *Journal of the American College of Cardiology* 59(12): 1058–1072.
- Ughi, G. J.; Adriaenssens, T.; Sinnaeve, P.; Desmet, W.; D'hooge, J. 2013. Automated Tissue Characterization of in Vivo Atherosclerotic Plaques by Intravascular Optical Coherence Tomography Images. *Biomedical Optics Express* 4(7): 1014–1030.
- Van Soest, G.; Regar, E.; Koljenovi, S.; van Leender, J. H.; Gonzalo, N.; van Noorden, S.; Okamura, T.; Bouma, B. E.; Tearney, G. J.; Oosterhuis, J. W.; Serruys, P. W.; van der Steen, A. F. W. 2010. Atherosclerotic Tissue Characterization in Vivo by Optical Coherence Tomography Attenuation Imaging. *Journal of Biomedical Optics* 15(1): 011105-011105.
- Virmani, R.; Kolodgie, F. D.; Burke, A. P.; Farb, A.; Schwartz, S. M. 2000. Lessons from Sudden Coronary Death: A Comprehensive Morphological Classification Scheme for Atherosclerotic Lesions. *Arteriosclerosis, Thrombosis, and Vascular Biology* 20(5): 1262–1275.
- Wagstaff, K. 2012. Machine Learning That Matters. Unpublished Manuscript. arXiv preprint arXiv: 1206.4656. Ithaca, NY: Cornell University Library.
- Wang, L., and Wu, H. I. 2007. *Biomedical Optics: Principles and Imaging*. Hoboken, N.J.: Wiley-Interscience.
- Wang, Z. 2012. Volumetric Quantification of Fibrous Caps Using Intravascular Optical Coherence Tomography. *Biomedical Optics Express* 3(6): 1413.
- Yabushita, H.; Bouma, B. E.; Houser, S. L.; Aretz, H. T.; Jang, I. K.; Schlendorf, K. H.; Shishkov, M.; Kang, D. H.; Halpern, E. F.; Tearney, G. J. 2002. Characterization of Human Atherosclerosis by Optical Coherence Tomography. *Circulation* 106(13): 1640–1645.
- Zhang, X. M.; McKay, C. R.; and Sonka, M. 1998. Tissue Characterization In Intravascular Ultrasound Images. *IEEE Transactions on Medical Imaging* 17(6): 889–899.
- Ronny Shalev**, Ph.D. has spent much of the past 21 years in executive positions including vice president of marketing and sales at Orbotech (NASDAQ: ORBK) where he managed sales and marketing teams, and director of worldwide program management at Marvell Semiconductor (NASDAQ: MRVL) where he managed the development of more than two hundred products. In the beginning of his career, he worked as a software developer at IBM. He founded a start-up company and acquired a significant amount of experience as an entrepreneur. Shalev attended Case Western Reserve University (Cleveland, OH) and holds a M.Sc. in electrical engineering and applied physics specializing in robotics and control, and a B.Sc. in electrical engineering and applied physics. He recently returned to CWRU and earned his Ph.D. specializing in medical imaging, machine learning, and visualization.
- Andrew M. Rollins**, Ph.D., is a professor of biomedical engineering and medicine at Case Western Reserve University. His research interests are the development and application of advanced biomedical optical technologies, especially optical coherence tomography (OCT), and including optical stimulation and imaging of electro-physiology. Current projects include the study of developmental cardiology and endoscopic imaging of cardiovascular disease and cancer.
- David L. Wilson**, Ph.D., is the Robert Herbold Professor of Biomedical Engineering and Radiology, Case Western Reserve University. His research has focused on biomedical image analysis in clinical and pre-clinical models as well as quantitative evaluation of image quality. In the last several years, he has focused on intravascular OCT imaging and cardiovascular applications. Wilson has been principal investigator on numerous federal and state grant awards, and has more than 130 peer-reviewed publications. He serves on editorial boards, NIH study sections, and conference organization committees. At CWRU, he has served as principal investigator on major development grants, the doctoral student NIH T32 Imaging training grant, and advisor to numerous graduate and undergraduate students. Wilson is a founder of BioInVision, Inc., which is commercializing cryo-imaging. Wilson received his Ph.D. in electrical engineering from Rice University, Houston, TX.
- Soumya Ray** is an associate professor in the Department of Electrical Engineering at Case Western Reserve University. He is interested in machine-learning theory and applications, reinforcement learning and planning, and natural language processing. He received his undergraduate degree from the Indian Institute of Technology, Kharagpur, followed by MS and Ph.D. in computer science from the University of Wisconsin, Madison.
- Hiram Bezerra** is an assistant professor of medicine at Case Western Reserve University School of Medicine, the director of the Cath Lab, and the medical director of the Cardiovascular Imaging Core Lab at University Hospitals – Case Medical Center. He received his MD degree from the School of Sciences of the Santa Casa de Misericórdia, and his Ph.D. from the University of São Paulo, Brazil.
- Daisuke Nakamura**, MD, is affiliated with the Harrington Heart and Vascular Institute, University Hospitals Case Medical Center, Case Western Reserve University in Cleveland, OH. He has stated that he has no financial interests related to this article.
- Setso Nishino**, MD, Ph.D., is affiliated with the Harrington Heart and Vascular Institute, University Hospitals Case Medical Center, Case Western Reserve University in Cleveland, OH. He has stated that he has no financial interests related to this article.